Multi-Scale Analysis of Effective Mechanical Properties of Porous 3D Woven Composite Materials

Sergio Fraile Izquierdo*, Federico Semeraro*, Marcos Acín†
AMA, Inc. at NASA Ames Research Center, Moffett Field, California

This work aims to compute and analyze the mechanical properties of 3D woven composite materials that share the same yarn structure but differ in their matrix porosity and yarn's fiber volume fraction. Assuming linear elastic behavior, NASA's PuMA software was used to characterize the different composites from their constituents' data, averaging their elastic properties in three main directions to obtain their effective orthotropic mechanical properties. This was performed in three steps: firstly, the porous matrix phase was analyzed at the micro-scale; then, these results were used, along with the mechanical properties of the fibers, to model the yarns at the meso-scale; finally, results from the constituents were homogenized and used to model the mechanical behavior of the unit cell at the macro-scale. The 3D woven composite materials selected for this study are made of a mixture of phenolic resin with porosity values between 0 and 0.6, and infiltrated carbon fiber yarns with fiber volume fractions between 0.5 and 0.8. Results from this study show the effect of different matrix porosities and fiber volume fractions on the macro-scale mechanical properties, and were validated through theoretical and semi-empirical expressions found in the literature.

I. Nomenclature

c	=	fitting constant [-]
d	=	pore diameter in voxels
E	=	Young's modulus [Pa]
G	=	shear modulus [Pa]
ROM	=	Rule of Mixtures
RVE	=	Representative Volume Element
TPS	=	Thermal Protection System
V	=	volume fraction [-]
ϵ	=	strain [-]
ν	=	Poisson's ratio [-]
ϕ	=	porosity [-]
ψ	=	maximum packing ratio [-]
ξ	=	Halpin-Tsai reinforcement parameter [-]

Subscripts :

1, 2, 3	=	directions X, Y and Z
f	=	fiber
L	=	longitudinal direction
m	=	matrix
T	=	transverse direction

*Research Scientist/Engineer, NASA Ames Thermal Protection Materials Branch
†Engineering Consultant, NASA Ames Thermal Protection Materials Branch

II. Introduction

Over the last decade, textile-reinforced composites have become crucial in the aerospace industry, replacing more traditional materials such as metals and ceramics in many applications. Their strong directional properties allow tailoring structures to their expected loading case while optimizing weight, giving engineers a wide variety of design options that can replace full assemblies of metal parts. Other advantages are their durability in harsh environments and high in-plane fatigue resistance. However, multilayered 2D composite materials suffer from poor inter-laminar mechanical properties and damage tolerance due to lack of through-the-thickness fibers [1] .

To address some of the issues that laminated composite materials present, three-dimensional (3D) textile composites have been developed for specific applications with multi-directional mechanical and thermal loads [2]. In 3D woven composites, reinforcement is also weaved through the thickness direction, which leads to enhanced out-of-plane mechanical properties. This reduces the delamination often experienced by 2D woven composites and decreases crack risks [3]. An example of a 3D woven composite material within NASA is the recently developed Heatshield for Extreme Entry Environment Technology (HEEET) shown in Fig. (1), a three-dimensional woven dual-layer carbon phenolic Thermal Protection System (TPS) material, designed to meet NASA's needs for planetary science missions with very high heating entry environments [4].

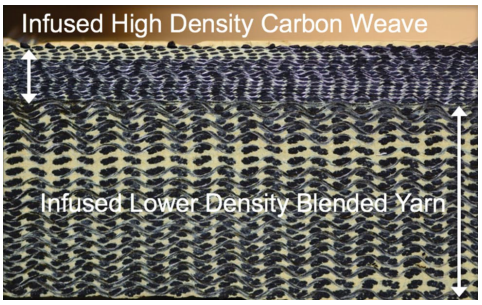

Fig. 1 HEEET cross-section [5]

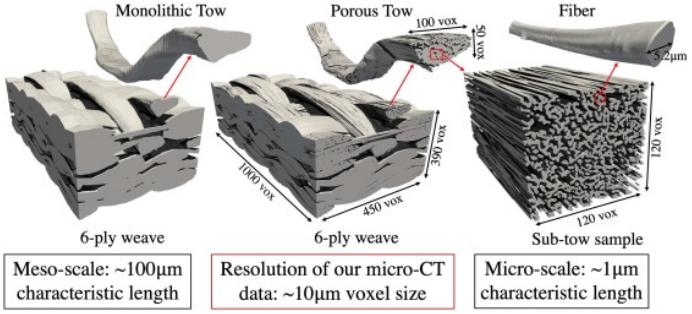

Fig. 2 Different scales in a woven material [6]

Designing a 3D woven material for a specific application is not trivial due to the high number of design options: constituents selection, resin infusion process, yarns structure, fiber volume fraction, curing process, and so on. This paper focuses on multi-scale modeling to obtain the mechanical properties of different 3D woven composites that share the same yarn structure but differ in their matrix porosity and fiber volume fraction. This approach could also be expanded to take into account other 3D weave structures to perform full design optimizations of 3D woven composites.

In order to obtain the mechanical properties of the materials investigated, the authors used the PuMA software [7–9], an open-source software used to perform the solid mechanics simulations. The software is able to either generate domains either artificially or imported from micro-CT scans and compute material properties such as: porosity, specific surface area, effective thermal conductivity, pore diameter, tortuosity, and permeability. New capabilities were added recently to carry out anisotropic analyses of fibrous and woven materials to estimate their local orientations and compute their effective conductivity following the Multi-Point Flux Approximation (MPFA) method [6, 10]. This paper takes advantage of the latest addition to this software, a finite volume anisotropic stress analysis solver based on the Multi-Point Stress Approximation (MPSA) method [11, 12]. For geometric modeling of textiles and composites materials, PuMA makes use of the open-source library TexGen [13].

The following section details the steps to obtain the mechanical properties at the micro-scale (porous resin), meso-scale (resin infiltrated yarns), and macro-scale (orthotropic unit cell). Section IV analyzes the mechanical properties obtained for the studied constituents and their corresponding 3D woven composite materials, and Section V summarizes the insights from this study and future work.

III. Methodology

The methodology followed to compute the mechanical properties of the 3D woven composites consists of breaking down the analysis into three steps. First, the porous phenolic resin is generated artificially to obtain its elastic constants. Then, these results are used along with the fiber's data to model the behavior of the yarns. Lastly, the results from the

constituents are used to solve the effective mechanical properties of their corresponding unit cell, which is the smallest repeatable pattern in the weave architecture. It is assumed that every unit cell in the 3D woven structure has a similar mechanical behavior, therefore the mechanical properties of the weave can be predicted by just modeling one unit cell with periodical boundary conditions, as explained in the next paragraphs.

PuMA's voxel-based stress analysis implementation for voxel grids is based on the MPSA method developed by Nordbotten et al. [11]. This approach is based on cell-centered discretizations for deformation and expresses the conservation of momentum in the finite volume sense, approximating the cell-face stress values following the multi-point approximation method [14]. The MPSA method is known to be convergent for a wide range of grids and effectively handles anisotropic materials with large jumps in mechanical properties [15].

The procedure to obtain the effective mechanical properties for any material with PuMA follows the Representative Volume Element (RVE) homogenization method [16], which consists of running six separate simulations: three for the normal cases, imposing a fixed displacement in each of the three directions (Dirichlet boundary condition), keeping the opposite face fixed, and applying the right boundary condition to the other four faces (symmetry, periodic, free), and another three simulations for the pure shear cases. By doing this, it is possible to solve the stress field generated in the material and obtain the anisotropic elasticity tensor. Having the anisotropic elasticity tensor and assuming orthotropic behavior of the material, it is possible to obtain the nine orthotropic effective mechanical properties (E_1, E_2, E_3, ν_{12}, ν_{23}, ν_{13}, G_1, G_2, G_3). This paper focuses on the cases with normal load conditions disregarding the pure shear cases, as they are easier to validate with expressions present in the literature.

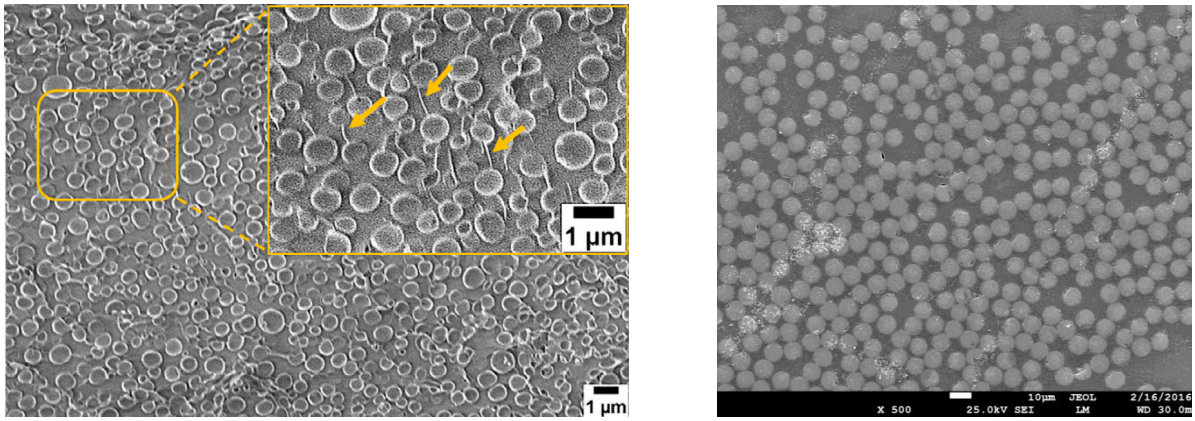

(a) Micrograph of cured porous phenolic resin [17] **(b) Micrograph of carbon fibers [18]**

Fig. 3 Microscopic images of porous phenolic resin and resin impregnated carbon fibers

The matrix phase for all 3D woven composites studied is made of phenolic resin with porosity (ϕ) values between 0 and 0.6. A micrograph of this material, in which it is possible to see the spherical pores, can be observed in Fig. (3a). On the other hand, the yarns are made of resin-impregnated carbon fibers, represented in Fig. (3b), with fiber volume fractions between 0.5 and 0.8. The following sub-sections explain how the mechanical properties of the constituents were modeled separately before solving their respective unit cell.

A. Matrix Modeling

The choice of phenolic resin as matrix phase in this study was motivated by its presence in TPS materials historically used by NASA. Non-porous carbon phenolic ablators were used on the Pioneer (Venus) and Galileo (Jupiter) entry probes [19, 20]; more recently, the highly porous phenolic-impregnated carbon ablator (PICA) was used for the Stardust, Mars Science Laboratory and Perseverance missions [21, 22]. In addition, future NASA missions with high heating entry environments are expected to use HEEET or 3MDCP [23], a new generation of 3D woven TPS materials impregnated with porous phenolic resin.

The function of the porous phenolic matrix in 3D woven TPS materials is to block the flow of hot gases going into the material and to insulate the internal surface from excessive temperatures. On the other hand, fibers are responsible for carrying the mechanical loads. Defects in the matrix component, such as voids and micro-cracks, are commonly

introduced during the manufacturing process and do not compromise the structural integrity. As a result, the porous material can fully satisfy the requirements to block flow and provide adequate insulation [24].

This paper analyzes the influence of porosity on the mechanical properties of the matrix and the weave's unit cell. The size and distribution of voids in phenolic resins can be controlled through the curing process by using catalysts and different cure cycles [17]. The porous phenolic resin models analyzed in this study have a porosity between 0 and 0.6 and were generated using a function included in PuMA to add intersecting random spherical voids to fully dense materials, as shown in Fig. (4). The following typical mechanical properties [17] were used for the fully dense isotropic phenolic resin: E = 4.5 GPa and $\nu = 0.3$.

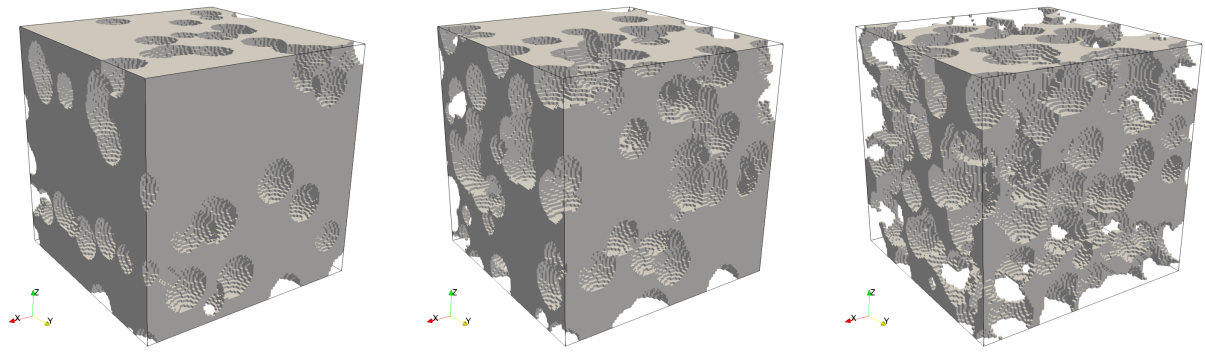

(a) $\phi = 0.2$ **(b)** $\phi = 0.4$ **(c)** $\phi = 0.6$

Fig. 4 Voxelized models of porous phenolic resin matrix

To make sure these models accurately represent the mechanical behavior of the material, a sensitivity analysis was carried out to minimize the uncertainty associated with the variability in pore distribution, and the effect of modeling the pores with voxels by varying the pore diameter. The grid size used for all models was $100 \times 100 \times 100$ voxels and the range of pore diameters studied range from 4 (coarser sphere) to 20 (smoother sphere) voxels, as shown in Fig. (5).

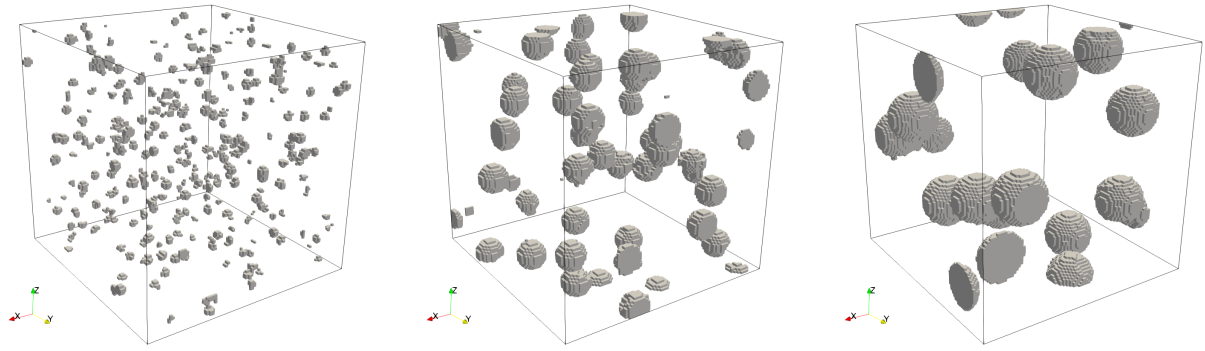

(a) Pores with d = 4 voxels **(b) Pores with d = 12 voxels** **(c) Pores with d = 20 voxels**

Fig. 5 Voxelized representation of different pore diameters

The relation between porosity and Young's modulus has been widely studied in the literature for certain materials and pore structures and the outcome from most of these analyses are fitting expressions based on experimental data [25–28]. Some of these studies include relationships for porous solids with spherical voids based on Eq. (1). Bert [29] proposed to use Eq. (1) accounting for the stress concentration factor, K, for an isolated void and the maximum porosity, ϕ_{max}, through the relation $c = K\phi_{max}$. He also stated that for materials with spherical voids following a hexagonal close-packed distribution, these parameters should have the values: $K = 2$ and $\phi_{max} = 0.7405$.

$$E_\phi = E_0 \left(1 - \frac{\phi}{\phi_{max}}\right)^c \tag{1}$$

More recently, Roberts [30] carried out a Finite Element Method (FEM) study to analyze how porosity and pore shape influence mechanical properties. He found that the Young's modulus for a solid with random overlapping spherical pores can also be modeled through Eq. (1) with the following empirical correlation parameters: $c = 1.65$ and $\phi = 0.818$. The results for the porous phenolic materials analyzed in this study are shown in Section IV.A, along with their comparison with the models from Bert and Roberts.

B. Yarn Modeling

The yarn models analyzed in this study are made of carbon fibers infiltrated with porous phenolic resin. This choice of constituents was also motivated by their ubiquitous presence in TPS materials used by NASA, as explained in Section III.A. Although this study only uses a single material for the fibers, with this methodology, it would also be possible to analyze the influence of blended yarns made of two or more different types of fibers, including different packing distributions and volume fractions.

Fibers in composite materials in general, and 3D woven materials in particular, are expected to carry most of the mechanical loads. To study the influence of different fiber-to-resin volume fractions within the yarns, they were modeled following a hexagonal packing structure with volume fractions between 0.5 and 0.8. Representative volume elements corresponding to these configurations can be observed in Fig. (6a), and these models were discretized into a voxel mesh of dimensions $25 \times 100 \times 173$ (X,Y Z) as shown in Figs. (6b, 6c). The mechanical properties used for the carbon fibers are as follows: $E_L = 230$ GPa, $E_T = 15$ GPa, $\nu_{LT} = 0.2$, $\nu_{TT} = 0.2$, and the mechanical properties used for the infiltrated phenolic resin were taken from the results of the porous matrix simulations for their respective porosity between 0 and 0.6.

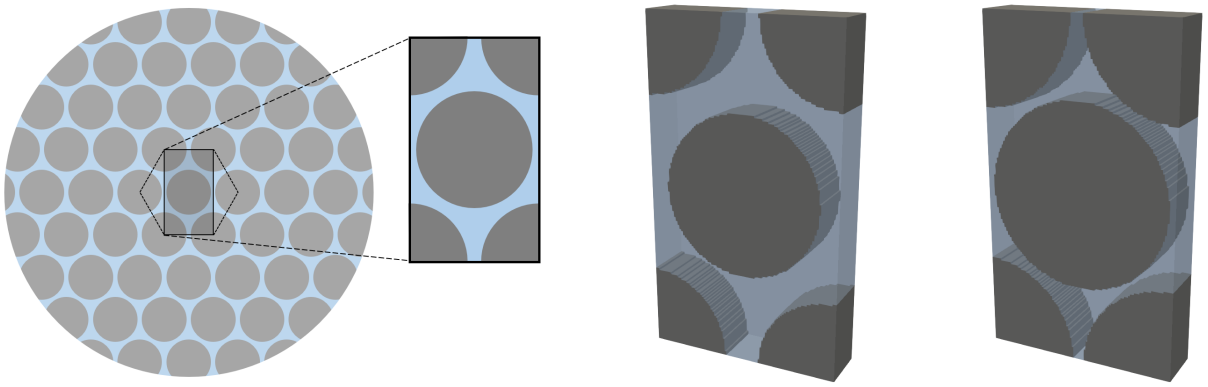

(a) Fibers distributed following a hexagonal packing **(b) Yarn RVE** ($V_f = 0.6$) **(c) Yarn RVE** ($V_f = 0.8$)

Fig. 6 Representation of the yarn models

The results were compared against the Rule of Mixtures (ROM) [31] to validate the mechanical properties computed for the yarns. This rule is a method to approximate properties of composite materials based on the assumption that a composite property is the volume weighted average of the properties of its constituents: fibers and infiltrated resin. The expressions for the ROM applied to mechanical properties can be observed in Eq. (2). It is generally accepted that results for the longitudinal component along the direction of the fiber, E_L and ν_{LT}, give accurate predictions. On the other hand, the transverse component, E_T, is usually underestimated and should be considered as the lower-bound modulus [32]. This is because the ROM model does not consider the shape of the fibers and their distribution.

$$E_L = E_{f_L} V_f + E_m V_m \qquad E_T = \frac{E_{f_T} E_m}{E_{f_T} V_f + E_m V_m} \qquad \nu_{LT} = \nu_{f_{LT}} V_f + \nu_m V_m \tag{2}$$

A better estimation of the Young's modulus for the transverse direction can be obtained with the Halpin-Tsai expression [33]. This equation was modified by Nielsen [34] to account for the maximum packing, ψ, as shown in Eq. (3). This formula also depends on the fiber distribution and shape through an empirical parameter, ξ, which is a measure of the reinforcement provided by the fibers. According to [35], for a hexagonal distribution of fibers, the following parameters should be used: $\psi = 0.907$ and $\xi = 1$. When $\psi = 1$, Nielsen's expression becomes Halpen-Tsai's.

$$E_T = E_m \frac{1 + \xi \eta V_f}{1 - \psi \eta V_f} \tag{3}$$

where,

$$\eta = \frac{r - 1}{r + \xi} \qquad r = \frac{E_{f_T}}{E_m} \tag{4}$$

Another approximation to the transverse Young's modulus was provided by Chamis [36] following an analytical micro-mechanics approach. Chamis' equations do not include any empirical parameters and are widely used due to their simplicity and greater accuracy compared to the ROM. The expression for the transverse Young's modulus can be observed in Eq. (5).

$$E_T = \frac{E_m}{1 - \sqrt{V_f}\left(1 - \frac{E_m}{E_{f_T}}\right)} \tag{5}$$

In Section IV.B the results from this study obtained with PuMA are compared with the theoretical and semi-empirical equations described above.

C. Unit Cell Analysis

After characterizing the different constituents involved in this study, their effective mechanical properties were used to feed the solid mechanics model of their respective materials. The unit cell structure, common to all 3D woven materials analyzed in this paper, is represented in Fig. (7b). It was discretized into a voxel mesh of dimensions $150 \times 150 \times 60$ (X,Y Z) after determining that a finer discretization increased the computation time while providing similar results, and the same methodology used at the micro-scale was applied to obtain the effective orthotropic mechanical properties of each material.

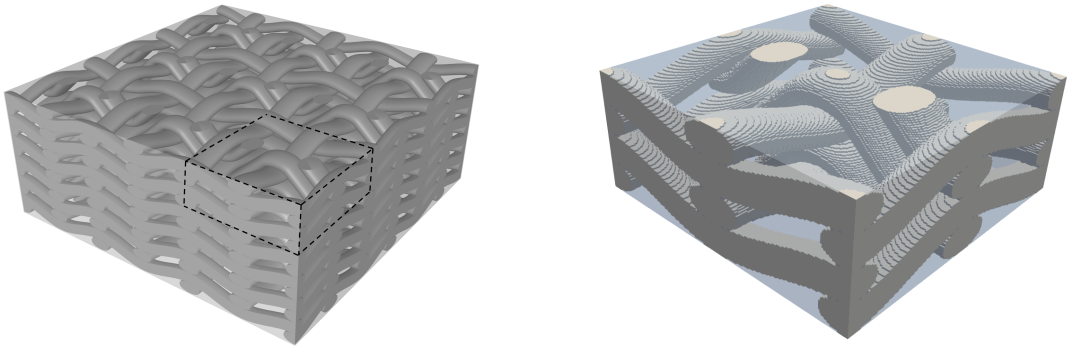

(a) 3D woven composite material **(b) Unit cell**

Fig. 7 Model of the studied 3D woven material and its corresponding voxelized unit cell

The results for the unit cell models can be found in Section IV.C. Differently from the constituents' properties, the validation of the RVE's properties against experimental data or FEM simulations is out of the scope of this study. Future work will focus on an in-depth analysis of PuMA's elasticity solver, including rigorous validation cases at the micro and macro-scales for a wide variety of materials and load conditions.

IV. Results

This section summarizes the results obtained for the different constituents and unit cell models following the methodology explained in Section III. As stated before, the scope of this study covers the first three simulations (normal cases) of the RVE homogenization method, so the effective mechanical properties analyzed are the Young's moduli and Poisson's ratios.

A. Matrix Results

A representation of some phenolic matrix simulations to obtain the components of the elasticity tensor in the X direction can be observed in Fig. (8). The top three sub-figures represent the internal displacement in the X direction after imposing a displacement to the X positive (right) face of one voxel ($\epsilon_x = 1\%$). The sub-figures at the bottom represent the stress field in the X direction associated with the imposed strain. As expected, an increase in porosity leads to an increase in the maximum stress value due to the higher stress concentration localized in some regions. As a result, the mechanical properties of the matrix models are expected to be highly dependent on their porosity values.

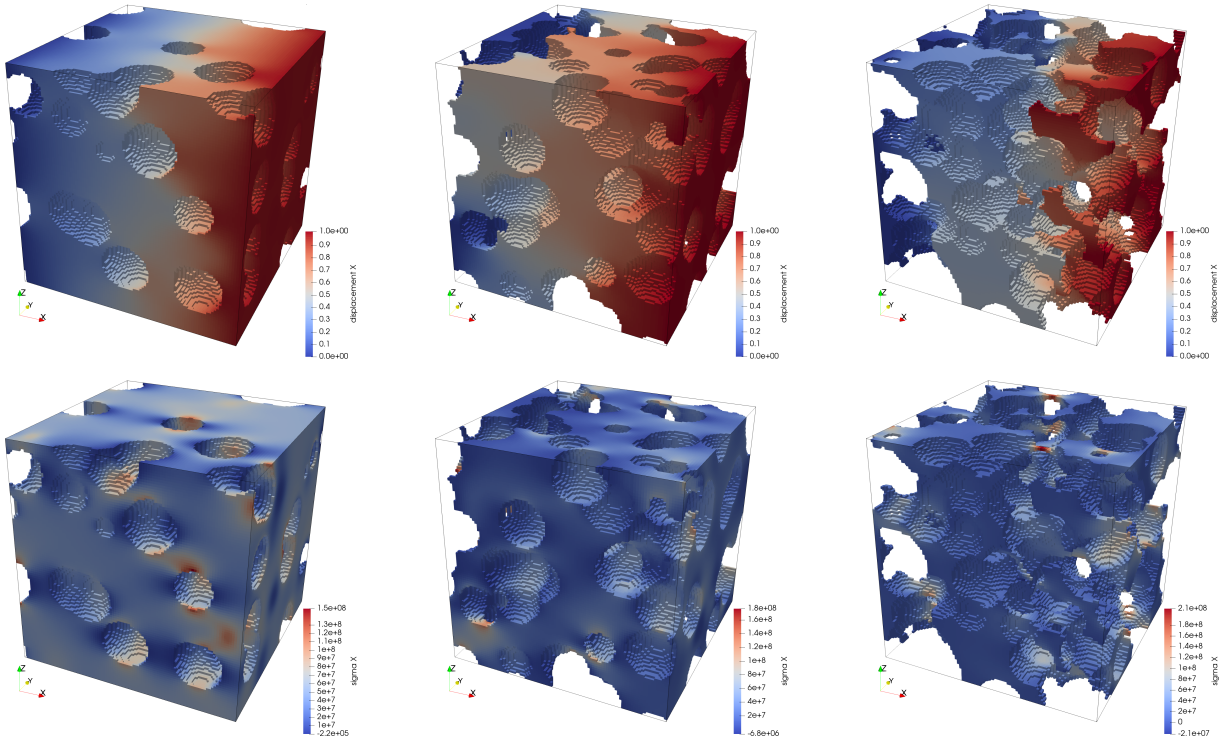

(a) $\phi = 0.2$ **(b)** $\phi = 0.4$ **(c)** $\phi = 0.6$

Fig. 8 Displacement (top) and direct stress (bottom) fields in the X direction for the porous phenolic matrix

The process of modeling porosity through a random distribution of porous voids introduces some level of variability in the results. To address this issue, up to 30 simulations were carried out for each one of the load cases, minimizing the uncertainty associated with this generation process down to a standard error <2% for all cases. In addition, since the voxel discretization of the pores may affect the results, a sensitivity analysis was carried out to assess the optimum pore diameter (in voxels) for this study. Results from this procedure are shown in Fig. (9a), which relates the Young's modulus of the porous phenolic with its pore diameter in voxels for three different porosities along with its standard deviation. According to these results, the Young's modulus decreases with pore coarseness (fewer number of voxels) for pore diameters between 4 and 16 voxels, and it plateaus for pore diameters >16 voxels. This can be explained by the fact that a finely discretized sphere has a lower stress concentration factor than a coarse one. For this reason, the pore diameter selected for this study is 20 voxels.

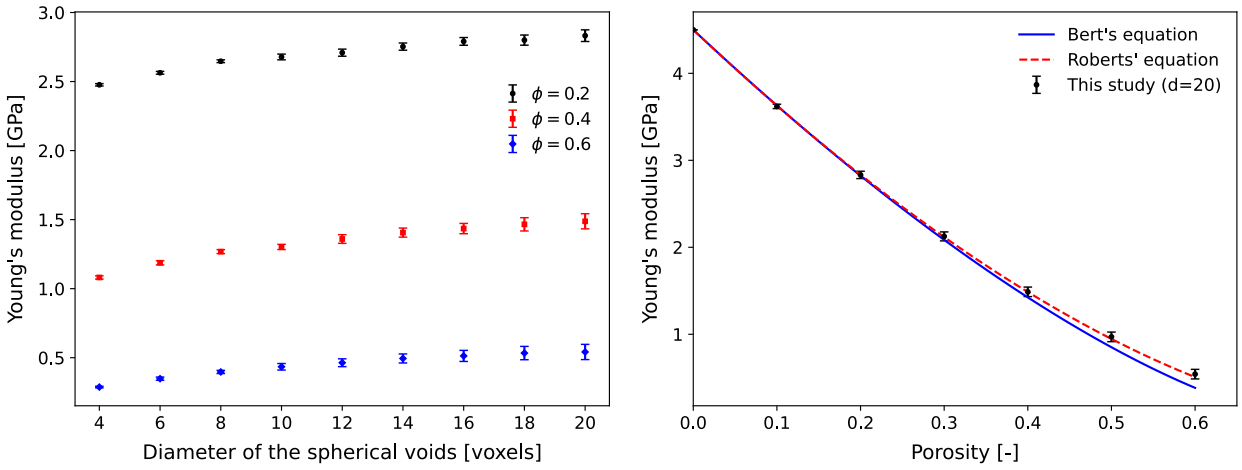

(a) Young's moduli for different pore diameters and porosities **(b) Young's moduli comparison for different porosities**

Fig. 9 Mechanical properties of the phenolic matrix for different porosities

According to Fig. (9), materials with higher porosity have lower Young's modulus. Data from Fig. (9b) shows a perfect agreement between the results from this study, obtained with PuMA, and Roberts' equation [30]. The maximum error between both is just 1.03% for the case with porosity 0.6. This study also shows a very good agreement with the expression from Bert [29], but the error at porosities >0.4 is noticeably higher.

B. Yarn Results

Figure (10) shows the internal stress distribution in the transverse direction (Z) after a forced displacement of one voxel imposed to the Z positive (top) face ($\epsilon_z = 0.578\%$) with periodic boundary conditions on the four sides. It is possible to observe the paths the stress follows through the matrix for the different fiber volume fraction cases. The higher concentration of stress happens in the case $V_f = 0.8$ due to the proximity between fibers, which leaves a narrower path for the stress through the phenolic resin.

There is no representation of the stress distribution in the longitudinal (X) direction because, as expected, for an imposed strain, all fibers share the same stress values and the matrix carries very little load. Due to this, the averaged effective mechanical properties should greatly vary with different fiber volume fraction values.

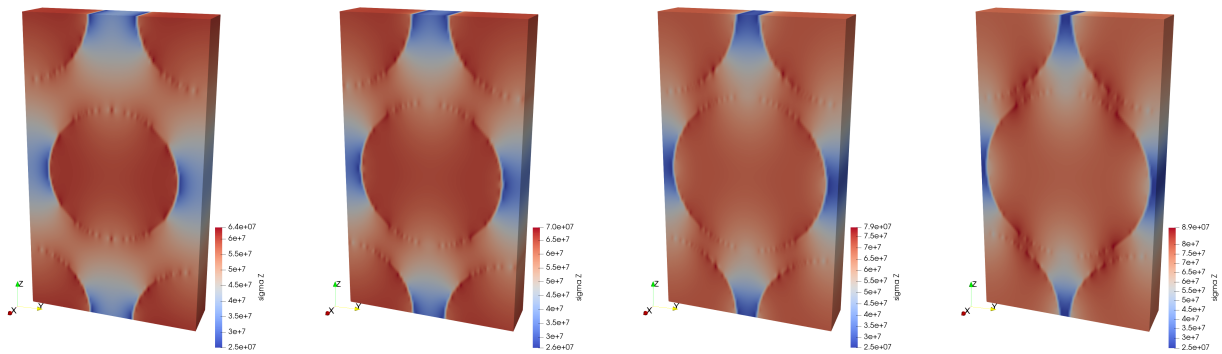

(a) $V_f = 0.5$ **(b)** $V_f = 0.6$ **(c)** $V_f = 0.7$ **(d)** $V_f = 0.8$

Fig. 10 Direct stress of the yarn in the transverse (Z) direction

Figure (11) shows the mechanical properties of the yarns obtained for the range of porosities and volume fractions studied. It is possible to observe in Fig. (11a) that the transverse Young's modulus increases with an increase in the fiber volume fraction of the yarn. This can be explained by the fact that the higher stiffness of the fibers acts as a

reinforcement. On the other hand, the porosity of the resin phase weakens the material in the transverse direction. These results were compared against the theoretical and semi-empirical equations explained in Section III.B. The expression from Halpin-Tsai [33] shows the best agreement with the results from this study at all fiber volume fractions, while the results from Nielsen [34] show good agreement for $V_f < 0.6$, and the equation from Chamis [36] shows a better agreement than Nielsen's at high fiber volume fractions.

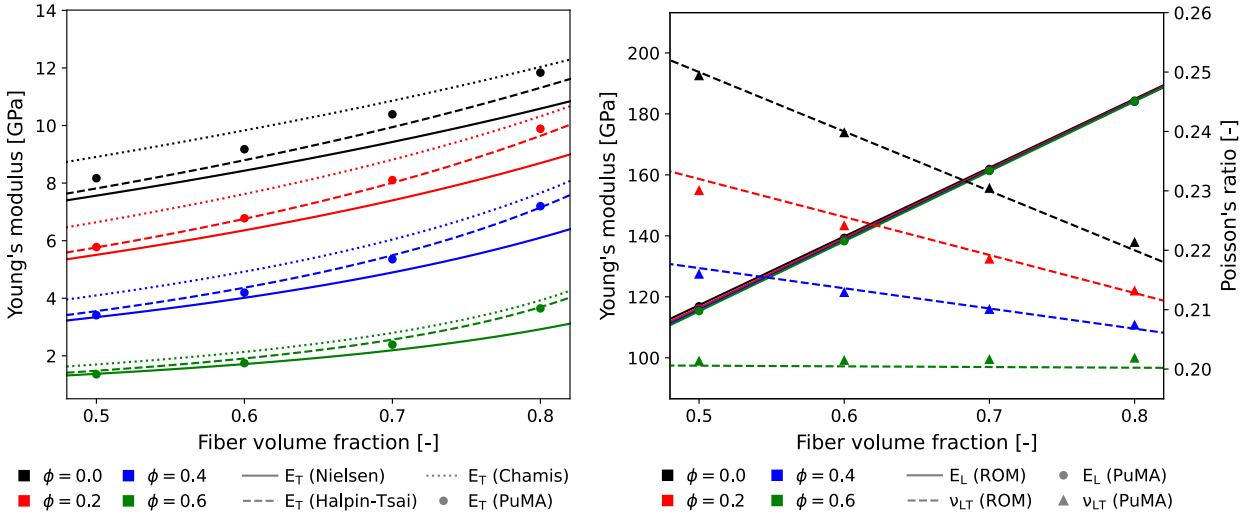

(a) Transverse Young's modulus **(b) Longitudinal Young's modulus and Poisson's ratio**

Fig. 11 Mechanical properties of the yarns for different porosities and fiber volume fractions

The longitudinal Young's modulus and the Poisson's ratio are represented in Fig. (11b). Both elastic constants show excellent agreement with the expressions from the ROM. The longitudinal Young's modulus is strongly connected with the fiber volume fraction of the yarns following a linear relation, and the porosity of the resin phase has little effect since the fibers carry most of the load. On the other hand, the Poisson's ratio is strongly dependent on both the fiber volume fraction and the porosity of the infiltrated phenolic resin.

C. Unit Cell Results

As explained in Section III.C, the same methodology used at the micro-scale for the constituents was applied to obtain the effective mechanical properties of the unit cell. Fig. (12) shows the internal stress distribution in X, Y, and Z directions under the different normal load conditions applied following the RVE homogenization method. The matrix phase is hidden for visualization purposes.

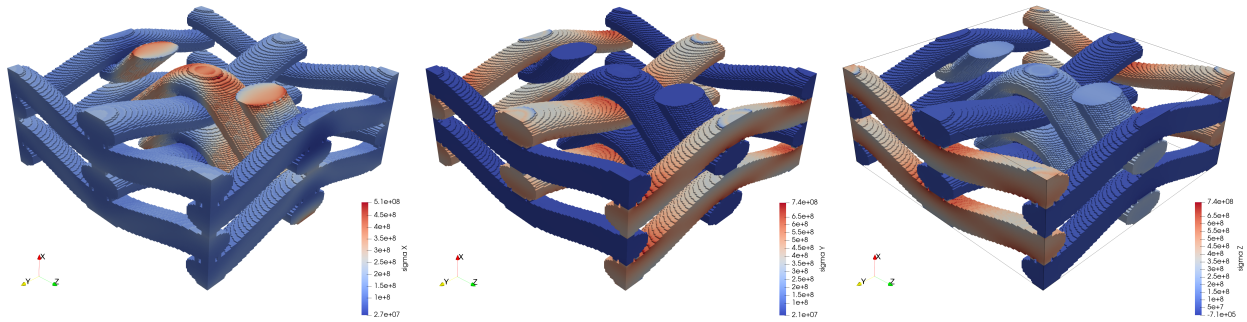

(a) Out-of-plane (X) direction **(b) In-plane (Y) direction** **(c) In-plane (Z) direction**

Fig. 12 Direct stress induced in the unit cell in the out-of-plane (X), and in-plane (Y, Z) directions

As expected, for the X case with the strain applied in the out-of-plane direction, Fig. (12a), the yarns weaved through the thickness (binder yarns) reinforce the matrix and contribute to the out-of-plane stiffness. On the other hand, for the the Y and Z cases, Figs. (12b, 12c), the yarns with the least crimp carry most of the loads.

The results for the Young's modulus in the three principal directions are represented in Fig. (13a) for all porosities and fiber volume fractions in the yarns. As it can be observed, the fiber volume fraction especially affects the directions Y (E_2) and Z (E_3), while the X (E_1) direction is mostly driven by the porosity of the phenolic resin. This means that in the through the thickness direction (X), not only the binder yarns but also the porous matrix has an important structural role. As expected, the highest Young's modulus corresponds to the Y (E_2) direction, which has the highest number of yarns with the least crimp.

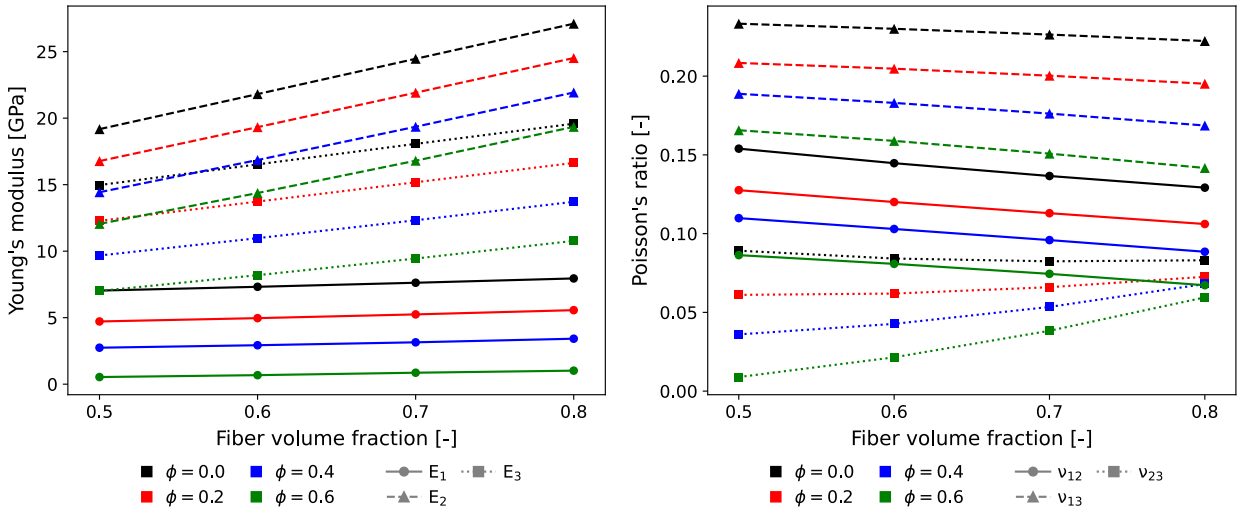

(a) Young's moduli of the unit cell

(b) Poisson's ratios of the unit cell

Fig. 13 Mechanical properties of the unit cell for different porosities and yarns' fiber volume fractions

The Poisson's ratios for all porosity and fiber volume fraction cases can be observed in Fig. (13b). The out-of-plane Poisson's ratios, ν_{12} and ν_{13}, present the highest values, are mainly affected by the porosity of the phenolic resin, and their value decrease when increasing the fiber volume fraction. On the other hand, the in-plane Poisson's ratio, ν_{23}, shows the opposite behavior and increases with the fiber volume fraction. This behavior is especially clear for high matrix porosity values.

V. Conclusion

This work described a methodology to carry out multi-scale analyses of porous 3D woven materials. Still, it can be applied to any type of composite material to obtain its homogenized orthotropic mechanical properties. The PuMA software allowed to firstly analyze the constituents at the micro-scale (matrix/yarns) and then use those results to accurately model the unit cell at the macro-scale for multiple yarn fiber volume fractions and matrix porosity values.

Results for the constituents and the unit cell were commented in Section IV, with regards to how different porosities and fiber volume fractions affect the mechanical behavior of the different materials studied. In addition, it was possible to validate the results for the porous matrix and the yarns by comparing them to analytical expressions listed in the literature.

Future work will extend the applicability of this study to the pure shear cases, and it will focus on an in-depth analysis of PuMA's elasticity solver, including rigorous validation cases for a wide variety of materials and load conditions.

Acknowledgments

The authors would like to thank Justin B. Haskins, Lauren J. Abbott, and Trenton M. Ricks for the useful discussions. This work is supported through contract NNA15BB15C to AMA, Inc. from the Entry Systems Modeling project (Michael D. Barnhardt project manager, Aaron M. Brandis principal investigator) as part of the NASA Game Changing Development program of NASA's Space Technology Mission Directorate.

References

[1] Karaduman, N. S., Karaduman, Y., Ozdemir, H., and Ozdemir, G., "Textile reinforced structural composites for advanced applications," *Textiles for advanced applications*, 2017, p. 87.

[2] Thuruthimattam, B., and Naik, N., "Mechanical characterization of hybridized 3D orthogonally woven composites," *39th AIAA/ASME/ASCE/AHS/ASC Structures, Structural Dynamics, and Materials Conference and Exhibit*, 1998, p. 1809.

[3] Chen, X., Taylor, L. W., and Tsai, L.-J., "An overview on fabrication of three-dimensional woven textile preforms for composites," *Textile Research Journal*, Vol. 81, No. 9, 2011, pp. 932–944.

[4] Ellerby, D., Driver, D., Gasch, M., Mahzari, M., Milos, F., Nishioka, O., Peterson, K., Stackpoole, M., Venkatapathy, R., Young, Z., et al., "Overview of Heatshield for Extreme Entry Environment Technology (HEEET) Project," 2018.

[5] Milos, F. S., Chen, Y.-K., and Mahzari, M., "Arcjet tests and thermal response analysis for dual-layer woven carbon phenolic," *Journal of Spacecraft and Rockets*, Vol. 55, No. 3, 2018, pp. 712–722.

[6] Semeraro, F., Ferguson, J. C., Panerai, F., King, R. J., and Mansour, N. N., "Anisotropic analysis of fibrous and woven materials part 1: Estimation of local orientation," *Computational Materials Science*, Vol. 178, 2020, p. 109631.

[7] Ferguson, J. C., Panerai, F., Borner, A., and Mansour, N. N., "PuMA: The porous microstructure analysis software," *SoftwareX*, Vol. 7, 2018, pp. 81–87.

[8] Ferguson, J. C., Semeraro, F., Thornton, J. M., Panerai, F., Borner, A., and Mansour, N. N., "Update 3.0 to "PuMA: The Porous Microstructure Analysis software",(PII: S2352711018300281)," *SoftwareX*, Vol. 15, 2021, p. 100775.

[9] Ferguson, J. C., Panerai, F., Lachaud, J., Martin, A., Bailey, S. C., and Mansour, N. N., "Modeling the oxidation of low-density carbon fiber material based on micro-tomography," *Carbon*, Vol. 96, 2016, pp. 57–65.

[10] Semeraro, F., Ferguson, J. C., Acin, M., Panerai, F., and Mansour, N. N., "Anisotropic analysis of fibrous and woven materials part 2: Computation of effective conductivity," *Computational Materials Science*, Vol. 186, 2021, p. 109956.

[11] Nordbotten, J. M., "Cell-centered finite volume discretizations for deformable porous media," *International journal for numerical methods in engineering*, Vol. 100, No. 6, 2014, pp. 399–418.

[12] Keilegavlen, E., and Nordbotten, J. M., "Finite volume methods for elasticity with weak symmetry," *International Journal for Numerical Methods in Engineering*, Vol. 112, No. 8, 2017, pp. 939–962.

[13] Zeng, X., Brown, L. P., Endruweit, A., Matveev, M., and Long, A. C., "Geometrical modelling of 3D woven reinforcements for polymer composites: Prediction of fabric permeability and composite mechanical properties," *Composites Part A: Applied Science and Manufacturing*, Vol. 56, 2014, pp. 150–160.

[14] Aavatsmark, I., "An introduction to multipoint flux approximations for quadrilateral grids," *Computational Geosciences*, Vol. 6, No. 3, 2002, pp. 405–432.

[15] Nordbotten, J. M., "Convergence of a cell-centered finite volume discretization for linear elasticity," *SIAM Journal on Numerical Analysis*, Vol. 53, No. 6, 2015, pp. 2605–2625.

[16] Omairey, S. L., Dunning, P. D., and Sriramula, S., "Development of an ABAQUS plugin tool for periodic RVE homogenisation," *Engineering with Computers*, Vol. 35, No. 2, 2019, pp. 567–577.

[17] Hamad, S. F., Farr, N., Fei, T., Shukor, N. F., Dean, J. S., Hayes, S. A., Foreman, J. P., and Rodenburg, C., "Optimizing size and distribution of voids in phenolic resins through the choice of catalyst types," *Journal of Applied Polymer Science*, Vol. 136, No. 47, 2019, p. 48249.

[18] Şahin, Y., and De Baets, P., "Tribological behaviour of unidirectional carbon fibre-reinforced epoxy composites," *IOP Conference Series: Materials Science and Engineering*, Vol. 174, IOP Publishing, 2017, p. 012009.

[19] Peterson, D. L., and Nicolet, W. E., "Heat shielding for Venus entry probes," *Journal of Spacecraft and Rockets*, Vol. 11, No. 6, 1974, pp. 382–387.

[20] Brewer, R., and Brant, D., "Thermal protection system for the Galileo mission atmospheric entry probe," *18th Aerospace Sciences Meeting*, 1980, p. 358.

[21] Willcockson, W. H., "Stardust sample return capsule design experience," *Journal of Spacecraft and Rockets*, Vol. 36, No. 3, 1999, pp. 470–474.

[22] Beck, R. A., Driver, D. M., Wright, M. J., Hwang, H. H., Edquist, K. T., and Sepka, S. A., "Development of the mars science laboratory heatshield thermal protection system," *Journal of Spacecraft and Rockets*, Vol. 51, No. 4, 2014, pp. 1139–1150.

[23] Ellerby, D., Hwang, H., Gasch, M., Beck, R., and White, T., "TPS and Entry Technologies for Future Outer Planet Exploration," *Bulletin of the AAS*, Vol. 53, No. 4, 2021.

[24] Langston, S., Peterson, K., and Poteet, C. C., "Effect of Phenolic Matrix Microcracking on the Structural Response of a 3-D Woven Thermal Protection System," *AIAA Scitech 2019 Forum*, 2019, p. 0162.

[25] Morrissey, L. S., and Nakhla, S., "A finite element model to predict the effect of porosity on elastic modulus in low-porosity materials," *Metallurgical and Materials Transactions A*, Vol. 49, No. 7, 2018, pp. 2622–2630.

[26] Ternero, F., Rosa, L. G., Urban, P., Montes, J. M., and Cuevas, F. G., "Influence of the Total Porosity on the Properties of Sintered Materials—A Review," *Metals*, Vol. 11, No. 5, 2021, p. 730.

[27] Ji, S., Gu, Q., and Xia, B., "Porosity dependence of mechanical properties of solid materials," *Journal of Materials Science*, Vol. 41, No. 6, 2006, pp. 1757–1768.

[28] Choren, J. A., Heinrich, S. M., and Silver-Thorn, M. B., "Young's modulus and volume porosity relationships for additive manufacturing applications," *Journal of materials science*, Vol. 48, No. 15, 2013, pp. 5103–5112.

[29] Bert, C. W., "Prediction of elastic moduli of solids with oriented porosity," *Journal of materials science*, Vol. 20, No. 6, 1985, pp. 2220–2224.

[30] Roberts, A. P., and Garboczi, E. J., "Elastic properties of model porous ceramics," *Journal of the American Ceramic Society*, Vol. 83, No. 12, 2000, pp. 3041–3048.

[31] Whitney, J. M., McCullough, R. L., et al., *Delaware Composites Design Encyc: Micromechanical Materials Model, Volume II*, CRC, 1990.

[32] Ghafaar, M. A., Mazen, A., and El-Mahallawy, N., "Application of the rule of mixtures and Halpin-Tsai equations to woven fabric reinforced epoxy composites," *JES. Journal of Engineering Sciences*, Vol. 34, No. 1, 2006, pp. 227–236.

[33] Halpin, J. C., "Effects of Environmental Factors on Composite Materials," Tech. rep., Air Force Materials Lab Wright-Patterson AFB OH, 1969.

[34] Nielsen, L. E., "Generalized equation for the elastic moduli of composite materials," *Journal of Applied Physics*, Vol. 41, No. 11, 1970, pp. 4626–4627.

[35] Krishnamachari, S. I., and Broutman, L., *Applied stress analysis of plastics: A mechanical engineering approach*, Springer Science & Business Media, 2013.

[36] Chamis, C. C., "Simplified composite micromechanics equations for hygral, thermal and mechanical properties," 1983.